

# Iterative Occlusion-Aware Light Field Depth Estimation using 4D Geometrical Cues

Rui Lourenço<sup>1,3</sup>, *Student Member, IEEE*, Lucas Thomaz<sup>1,2</sup>, *Member, IEEE*, Eduardo A. B. Silva<sup>3</sup>, *Senior Member, IEEE*, and Sergio M. M. Faria<sup>1,2</sup>, *Senior Member, IEEE*

**Abstract**—Light field cameras and multi-camera arrays have emerged as promising solutions for accurately estimating depth by passively capturing light information. This is possible because the 3D information of a scene is embedded in the 4D light field geometry. Commonly, depth estimation methods extract this information relying on gradient information, heuristic-based optimisation models, or learning-based approaches. This paper focuses mainly on explicitly understanding and exploiting 4D geometrical cues for light field depth estimation. Thus, a novel method is proposed, based on a non-learning-based optimisation approach for depth estimation that explicitly considers surface normal accuracy and occlusion regions by utilising a fully explainable 4D geometric model of the light field. The 4D model performs depth/disparity estimation by determining the orientations and analysing the intersections of key 2D planes in 4D space, which are the images of 3D-space points in the 4D light field. Experimental results show that the proposed method outperforms both learning-based and non-learning-based state-of-the-art methods in terms of surface normal angle accuracy, achieving a Median Angle Error on planar surfaces, on average, 26.3% lower than the state-of-the-art, and still being competitive with state-of-the-art methods in terms of Mean Squared Error  $\times 100$  and Badpix 0.07.

**Index Terms**—Light Fields, Depth Estimation, 4D Geometry, Surface Normals

## I. INTRODUCTION

THE explosion of public and academic interest in Augmented and Virtual Reality applications in recent years [1], [2] has prompted the development of advanced imaging techniques to enhance the immersive experience. Among these techniques, light field cameras and multi-camera arrays have gained significant attention due to their ability to capture rich spatial and angular information about a scene. By recording the light rays from multiple viewpoints, these devices enable several applications, from the construction of new points-of-view for a given scene and refocusing of an image to the estimation of the depth of a scene, enabling 3D reconstruction applications. Most importantly, the dense capture of information is used in several computer vision applications, such as automatic measurements and quality control in different types of industries [3], post-processing

effects on photographs [4], and even the diagnostic of severe medical conditions, such as skin cancer [5].

Light field disparity estimation is crucial in many typical applications of light field technology. Unlike other depth estimation technologies, such as structured light [6] and Light Detection and Ranging (LiDAR) [7] systems, light field disparity estimation does not struggle in low lighting conditions as it does not rely on active sensors. Furthermore, due to most light fields' narrow baseline, light field-based methods can overcome the limitations of traditional stereo-vision approaches, increasing accuracy.

The best performing state-of-the-art methods for light field disparity estimation primarily rely on supervised learning models, such as [8]–[13]. These methods provide highly accurate results for the available computer-generated light field datasets, obtaining very good results in terms of most objective accuracy metrics, such as the Mean Squared Error (MSE) or Badpix 0.07, as defined in [14]. However, these models often focus on optimising sample-wise accuracy, neglecting other important metrics such as the geometric concordance of the results, as measured by the accuracy of surface normals estimated from the resultant depth maps, particularly on planar surfaces. This can result in common inaccuracies such as staircase effects or rugged planar surfaces when the resultant disparity maps are used for 3D reconstruction.

Other state-of-the-art methods tend to narrow the focus to 2D cuts of the entire 4D light field, referred to as Epipolar Plane Images (EPIs) [15]–[24], or operate based on energy cost models that avoid some of the known limitations for light field disparity estimation through different sets of heuristics [25]–[33]. Whilst some of these methods obtain competitive results, they tend to fall behind learning-based methods in terms of objective accuracy metrics. Furthermore, none of these approaches builds a cohesive mathematical model integrating the full four-dimensional complexity of the 4D light field.

This paper proposes relevant contributions to light field technology, in general, and to light field depth estimation, in particular, by providing a general geometric framework for translating between 4D-light-field space and 3D space. To that end, it formalises the concepts of a 4D Point-Projection Plane (4D-PPP), which is the image of a 3D-space point in the 4D light field, and studies the sampling of such planes from discrete light field images. While aspects of these concepts have been previously used in light field disparity estimation, it is the belief of the authors that their further investigation can bring valuable insights to light field imaging. Furthermore, inherent limitations of light field depth estimation are addressed

<sup>1</sup> Instituto de Telecomunicações, Portugal

<sup>2</sup> ESTG - Polytechnic University of Leiria, Leiria, Portugal

<sup>3</sup> PEE, COPPE, Federal University of Rio de Janeiro, Rio de Janeiro, Brazil

This work was supported by the Fundação para a Ciência e a Tecnologia (FCT), Portugal under PhD Grant 2020.05635.BD, Programa Operacional Regional do Centro, and by FCT/MCTES through national funds and when applicable co-funded by EU funds under the project UIDB/EEA/50008/2020 and LA/P/0109/2020.



Figure 1: Truncated horizontal EPI from the Cotton light field. The red line indicates the projection of a single 3D-space point.

in detail, such as occlusions, non-Lambertian scenes, regions with low texture variance in the scene, and the locality of photometric consistency-based models.

To assess the geometric foundations underlying these concepts, they are used as the basis for an Iterative Occlusion-Aware Depth Refinement (IOADR) algorithm that explicitly handles occlusions and surface normal accuracy. The IOADR algorithm outperforms the current state-of-the-art in terms of surface normal angle accuracy in planar regions.

The remainder of this paper is organised as follows: Section II provides a background of related work in light field disparity estimation and highlights the limitations of existing approaches. Section III presents the 4D-Point-Projection Plane, the geometric framework underlying the proposed algorithm, and analyses the limitations of this approach for disparity estimation. Section IV presents the proposed disparity refinement model and the associated optimisation algorithms, including a novel plane geometry cost based on surface normal estimation, and a novel occlusion detection algorithm. Section V presents a comparative experimental evaluation and ablation studies. Finally, Section VI concludes the paper, and outlines potential avenues for future research.

## II. BACKGROUND

Levoy and Hanrahan [34] were the first to propose the 4D light field as a simplified parameterisation of the plenoptic function using only 4 dimensions, known as *light slab*, or simply the two plane parameterisation. According to this model, the position in the first plane is represented by vector  $\mathbf{s} = [s \ t]^T$ , sometimes known as the angular position, and the position in the second plane has coordinates  $\mathbf{u} = [u \ v]^T$ , sometimes referred to as the spatial position. As such, a position in the continuous light field is given by a 4-dimensional vector  $\mathbf{r}$ :

$$\mathbf{r} = [\mathbf{u}^T \ \mathbf{s}^T]^T = [u \ v \ s \ t]^T. \quad (1)$$

In the remainder of this paper, this parameterisation of the plenoptic function is designated as the continuous light field function:

$$\mathcal{L} : \mathbb{R}^4 \rightarrow \mathbb{R}^3, \text{ s.t. } \mathbf{c} = \mathcal{L}(\mathbf{r}), \quad (2)$$

where the vector  $\mathbf{c} = [c_r \ c_g \ c_b]^T$  represents the colour of the light field in a given position.

Epipolar Plane Images (EPIs) are 2D slices of the light field that are parallel to either the  $s \times u$  or  $t \times v$  planes. An example of an  $s \times u$  EPI is shown in Figure 1. These EPIs reveal an important property of light fields, as the intersection of the image of a 3D-space point  $P$  in the light field  $\mathcal{L}(u, v, s, t)$  with any EPI is a straight line (shown in red in Figure 1) with an angular coefficient that is a function of the depth of  $P$  [35].

Such properties have been used extensively in the literature to estimate the depths of a 3D scene from light fields. In what follows, three classes of such methods are highlighted: Gradient-based [15]–[22], energy-model-based [23], [25]–[33], and supervised-learning-based [8]–[10].

### A. Gradient-based methods

Gradient-based methods work by directly estimating the gradient of the geometric structures present in EPIs. This strategy permits depth estimation over a continuous range by determining the angular coefficients of slanted lines in EPIs. However, unless supplemented by post-processing or further optimisation steps, they tend to achieve low accuracy in occluded regions.

An early approach to light field disparity estimation was to directly compute the gradient of EPIs [15]. More robust approaches make use of the Structure Tensor [36] as a tool that not only measures the direction of the slanted lines in EPIs but also provides a reliability metric for this calculation.

Wanner et al. [16] improve the structure tensor accuracy by calculating disparity using both horizontal and vertical EPIs. Rudin et al. [37] proposed a fast Total-Variation-Denoising-based scheme and a global optimisation process. Li *et al.* [18], improved this scheme by introducing a penalty metric that weights the reliability measure, in a way that improves performance in occlusion regions. Lourenço *et al.* [20] further enhanced this paradigm by explicitly comparing the disparity and texture edge maps, in-painting the disparity map with corrected values when a mismatch is found.

While such methods provide sizeable improvements relative to the base structure tensor, most post-processing improvements and optimisations lack robustness, enlarging silhouettes or introducing algorithmic artefacts.

### B. Energy-model-based methods

Energy-model-based methods create an energy model based on a cost function that should be minimal when the correct depth value is chosen. This minimisation is usually done by building a 3D cost-volume that consists of the costs, according to the energy model, of all combinations of pixel coordinates in a view and a finite set of different disparity labels. Obtaining a disparity map for a view is as simple as finding the disparity label that minimises this cost for each pixel.

Several cost metrics have been introduced based on the constraints of cost-volume minimisation. One of the earliest models, proposed by Tao *et al.* [25], combined two different metrics, defocus and correspondence, to provide somewhat accurate results. Lin *et al.* [27] improved this approach by refining the energy model. Jeon *et al.* [26] used Fourier analysis and a phase-shift system to build a cost-volume with sub-pixel accuracy. However, all of these methods have issues in the presence of occlusion regions.

Wang *et al.* [28] directly improved on [25] by relying on edge estimation to model occlusions explicitly. Strecke *et al.* [30] improved on [27] by both altering the model to be better behaved in occlusion regions and introducing a joint depth and normal map regularisation. Zhang *et al.* [23]

proposed the Spinning Parallelogram Operator (SPO), which extends the simple compass operator [38]—an edge detection and characterisation algorithm—to the EPI domain, obtaining encouraging results even in occlusion regions.

Williem *et al.* [31] introduced an entropy-based data cost resilient to occlusions, whereas Kang *et al.* [33] introduced an occlusion-aware voting cost that models occlusions by detecting colour inconsistencies in angular patches. Schilling *et al.* [24] achieved notable results by foregoing the cost-volume and, instead, following a local optimisation framework that supports more complex occlusion models, which take into account the depth of nearby pixels.

### C. Supervised-learning-based methods

More recently, supervised machine-learning approaches have gained some popularity for depth estimation. In general, these works rely on the 4D geometric properties of light fields to adapt existing machine-learning frameworks to the task of estimating depth from light fields.

Shin *et al.* [8] proposed EPI-net, a fully Convolutional Neural Network (CNN) built using a multi-stream network design where each stream receives views with a consistent baseline. The views on each stream are organised as view stacks, which can also be understood as stacked EPIs. As a supervised learning method, EPI-net requires a training set of light fields with a labelled ground truth. As there is a limited amount of such data, light field-specific data augmentations are used to facilitate training, such as shifting the centre of the light field view matrix and carefully rotating light field images.

Tsai *et al.* proposed AttNet [9], which consists of a convolutional neural network with an attention module, while Yan *et al.* [11] improve on this architecture by using light field edges as guidance. Kunyan *et al.* [10] presents an end-to-end fully convolutional network developed explicitly to estimate the depth value from the orientation of lines on EPIs, taking into account the coherence of relations between such lines. Han *et al.* [12] extracts the sequential features of EPIs by substituting CNNs with Recursive Neural Networks.

Supervised learning-based methods present some of the best results known to date in terms of estimation accuracy. These methods require a large database of images with annotated ground truth to avoid over-fitting issues, which tends to be an issue given the limited availability of light field databases. Although this problem is likely to diminish in relevance as light field technology rises in prominence, it is important to notice that the best learning-based methods for depth estimation using light fields make use of concepts derived from non-learning-based depth estimation methods [9], [11], [12]. Therefore, there is still a considerable impetus to keep investigating non-learning-based approaches to depth estimation, as well as refining its base geometric descriptions.

## III. THE 4D POINT-PROJECTION PLANE

One of the goals of light field analysis is to obtain a 3D representation of the scene being captured. To this end, one starts by determining the image of a 3D-space point on the 4D light field.

The image of a 3D-space point  $\mathbf{x} = [x \ y \ z]^T$  in a light field view associated with a camera with centre  $\tilde{\mathbf{s}} = [s \ t \ 0]^T$ , parallel to the  $x \times y$  plane and with a focal distance of  $D$  is the vector

$$\tilde{\mathbf{u}}' = \mathbf{x} + (\tilde{\mathbf{s}} - \mathbf{x}) \left( \frac{z - D}{z} \right). \quad (3)$$

Note that if the sensor plane is positioned between the camera centre and the object, then  $D > 0$ . If the camera centre is positioned between the object and the sensor plane, then  $D < 0$ .

If one wants a 3D-space point  $\mathbf{a} = [0 \ 0 \ Z_p]^T$  at depth  $Z_p$  to be always mapped to the origin of any view, the image  $\mathbf{o}$  of  $\mathbf{a}$  (computed from Eq. (3) for  $\mathbf{x} = \mathbf{a}$ ) should be made the origin of a view, which, from Eq. (3) yields the coordinates

$$\tilde{\mathbf{u}} = \tilde{\mathbf{u}}' - \mathbf{o} = D \left( \frac{1}{Z_p} - \frac{1}{z} \right) \tilde{\mathbf{s}} + \frac{D}{z} \left( \mathbf{x} - \mathbf{a} \frac{z}{Z_p} \right). \quad (4)$$

Since  $\mathbf{a} \frac{z}{Z_p} = [0 \ 0 \ z]^T$ , the above equation becomes

$$\tilde{\mathbf{u}} = D \left( \frac{1}{Z_p} - \frac{1}{z} \right) \tilde{\mathbf{s}} + \frac{D}{z} [x \ y \ 0]. \quad (5)$$

Noting that in the above equation all the vectors in  $\mathbb{R}^3$  have their  $z$  coordinates equal to zero, using the  $\mathbb{R}^2$  vectors  $\mathbf{u}$  and  $\mathbf{s}$  from Eq. (1), it becomes

$$\mathbf{u} = D \left( \frac{1}{Z_p} - \frac{1}{z} \right) \mathbf{s} + D \frac{\boldsymbol{\xi}^{(x \times y)}(\mathbf{x})}{z}, \quad (6)$$

where the 2D vector  $\boldsymbol{\xi}^{(x \times y)}(\mathbf{x}) = [x \ y]^T$  is the projection of the 3D-space point  $\mathbf{x}$  on the  $x \times y$  plane.

Referring to Eq. (1), a position in the continuous light field is given by a vector  $\mathbf{r} = [\mathbf{u}^T \ \mathbf{s}^T]^T \in \mathbb{R}^4$ . Then, the linear relation between the vectors  $\mathbf{s}$  and  $\mathbf{u}$  in Eq. (6) represents a 2D plane in the 4D light field space.

From the above, the image in the 4D light field of a 3D-space point  $\mathbf{x}$  will be a 2D plane as given by Eq. 6. This plane is referred to as a 4D Point-Projection Plane (4D-PPP), and it can be defined by three parameters. One parameter is its orientation  $\theta$ , defined as

$$\tan \theta = D \left( \frac{1}{Z_p} - \frac{1}{z} \right), \quad (7)$$

that, given the light field acquisition parameters  $D$  and  $Z_p$ , depends only on the depth  $z$  of the 3D-space point being imaged. The other two parameters determine its position in the 4D space, which are given by the vector  $\frac{D}{z} \boldsymbol{\xi}^{(x \times y)}(\mathbf{x})$ . Therefore, estimating the depth map of a 3D scene based on an acquired light field is equivalent to finding the angles  $\theta$  of the 4D-PPPs corresponding to the 3D-space points of the scene.

### A. 4D Point-Projection Planes in Discrete Light Fields

The light fields used in practice are sampled versions of the continuous light fields. In this work, a discrete light field  $\mathbf{L}(\mathbf{m}, \mathbf{k})$  is derived from Eq. (2) as

$$\mathbf{L}(\mathbf{m}, \mathbf{k}) = \mathcal{L} \left( \Delta \mathbf{u} \odot (\mathbf{m} - \mathbf{m}_r), \Delta \mathbf{s} \odot (\mathbf{k} - \mathbf{k}_r) \right), \quad (8)$$

where the operator  $\odot$  is the element-wise Hadamard product,  $\mathbf{m} = [m \ n]^T \in \mathbb{Z}^2$  and  $\mathbf{k} = [k \ l]^T \in \mathbb{Z}^2$ ,  $\Delta \mathbf{s} = [\Delta s \ \Delta t]^T \in \mathbb{R}^2$  provides the horizontal and vertical base-lines,  $\Delta \mathbf{u} = [\Delta u \ \Delta v]^T \in \mathbb{R}^2$  provides the dot pitches, the metric distance between pixels of each view,  $\mathbf{m}_r = [m_r \ n_r]^T \in \mathbb{Z}^2$  indicates the horizontal and vertical indexes of the origin of the views, and  $\mathbf{k}_r = [k_r \ l_r]^T \in \mathbb{Z}^2$  indicates the horizontal and vertical indexes of the reference view. From this definition, a discrete light field sample  $\mathbf{p} \in \mathbb{Z}^4$  can be computed from a real-world position  $[\mathbf{u}^T \ \mathbf{s}^T]^T \in \mathbb{R}^4$  using:

$$\mathbf{p} = \begin{bmatrix} \mathbf{m} \\ \mathbf{k} \end{bmatrix} = \begin{bmatrix} \lfloor \mathbf{u} \odot \Delta \mathbf{u} + \mathbf{m}_r \rfloor \\ \lfloor \mathbf{s} \odot \Delta \mathbf{s} + \mathbf{k}_r \rfloor \end{bmatrix}, \quad (9)$$

where the operator  $\lfloor \cdot \rfloor$  represents an element-wise rounding operation and the operator  $\odot$  represents the element-wise Hadamard division operator.

In some parts of this work, when describing geometric features in the discrete 4D light field, it will be necessary to reference positions with non-integer coordinates, outside its discrete grid. For this reason, normalised continuous coordinates  $\bar{\mathbf{r}} \in \mathbb{R}^4$  are defined such that:

$$\bar{\mathbf{r}} = \begin{bmatrix} \bar{\mathbf{u}} \\ \bar{\mathbf{s}} \end{bmatrix} = \begin{bmatrix} \mathbf{u} \odot \Delta \mathbf{u} + \mathbf{m}_r \\ \mathbf{s} \odot \Delta \mathbf{s} + \mathbf{k}_r \end{bmatrix}. \quad (10)$$

This real-valued extension of the discrete coordinates defined in Equation (9), together with Eq. (7), allows the description of Equation (6) as:

$$\begin{aligned} \bar{\mathbf{u}} &= \boldsymbol{\eta} \odot (\bar{\mathbf{s}} - \mathbf{k}_r) \tan \theta + D \frac{\xi^{(x \times y)}(\mathbf{x})}{z} \odot \Delta \mathbf{u} + \mathbf{m}_r \\ &= \boldsymbol{\eta} \odot (\bar{\mathbf{s}} - \mathbf{k}_r) \tan \theta + \bar{\mathbf{u}}_0, \end{aligned} \quad (11)$$

where  $\boldsymbol{\eta} = \begin{bmatrix} \frac{\Delta s}{\Delta u} & \frac{\Delta t}{\Delta v} \end{bmatrix}^T \in \mathbb{R}^2$  is referred to as the sampling slope distortion, and  $\bar{\mathbf{u}}_0$  represents the pixel position where the 4D Point-Projection-Plane intersects the reference view.

It is common in the literature to express the orientation of the 4D-PPP in terms of the disparity, that is, the variation of pixel positions in a view relative to a unit variation in view position  $\Delta \bar{\mathbf{s}} = [1 \ 1]^T$ . As such, from Eq. (11), if  $\bar{\mathbf{u}} = [\bar{u} \ \bar{v}]^T$ , the disparity  $\mathbf{d} = [d_u \ d_v]^T$  can be expressed as:

$$\mathbf{d} = \boldsymbol{\eta} \tan \theta. \quad (12)$$

### B. The 4D Point-Projection Image

Since the image of a 3D-space point in the continuous 4D light field is the 4D-PPP, it is helpful to identify the samples of the discrete 4D light field that belong to a given 4D-PPP. However, any of the discrete 4D samples of the light field are unlikely to belong to this plane. A simple approach to sample the 4D-PPP is, for each view indexed by  $\mathbf{k} \in \mathbb{Z}^2$ , to compute the normalised continuous coordinate  $\bar{\mathbf{u}} \in \mathbb{R}^2$  using Eq. (11) for  $\bar{\mathbf{s}} = \mathbf{k}$  and interpolate view  $\mathbf{L}(\mathbf{m}, \mathbf{k})$  in Eq. (8). This way, the spatially interpolated Light Field  $\bar{\mathbf{L}}(\bar{\mathbf{u}}, \mathbf{k})$  is generated. In this work, the views are interpolated to a sub-pixel spatial

position  $\bar{\mathbf{u}}$  using separable bi-linear interpolation [39] within each view.

From the above, the 4D Plane-Projection Image  $\mathbf{I}_{\theta, \bar{\mathbf{u}}_0}(\mathbf{k})$ , with dimensions equal to the horizontal and vertical number of views of the discrete 4D light field, can be defined as:

$$\mathbf{I}_{\theta, \bar{\mathbf{u}}_0}(\mathbf{k}) = \bar{\mathbf{L}}(\boldsymbol{\eta} \odot (\mathbf{k} - \mathbf{k}_r) \tan \theta + \bar{\mathbf{u}}_0, \mathbf{k}), \quad \text{for } \mathbf{k} \in \mathcal{A}, \quad (13)$$

where  $\mathcal{A}$  is the set of all views of the discrete 4D light field.

Thus,  $\mathbf{I}_{\theta, \bar{\mathbf{u}}_0}(\mathbf{k})$  is the result of sampling the 4D-PPP with orientation  $\theta$  that intersects the reference view at pixel  $\bar{\mathbf{u}}_0$ , at every interpolated view of the 4D discrete Light Field. It is important to note that if the surface to which the 3D-space point belongs to is Lambertian and the 3D-space point is visible across all views, its corresponding 4D Point-Projection Image (4D-PPI) should have the same colour across all views. In other words, a 4D-PPI should demonstrate photometric consistency [40].

The statement above implies that if a given 4D-PPI is not photometrically consistent, then at least one of the following happens:

- (i) the Lambertian assumption does not hold;
- (ii) the object is occluded in some views of the light field;
- (iii) the parametrization of the 4D-PPP does not match the true position of the 3D-space point represented in the pixel at position  $\bar{\mathbf{u}}_0$  of the reference view.

Since Eq. (7) means that finding the correct parametrization of the 4D-PPP is equivalent to finding the depth of the corresponding 3D-space point, from the above, one can infer the usefulness of developing cost models that attempt to quantify photometric consistency. A straightforward example of such a metric is the variance of the colours of all pixels of a given 4D-PPI. A more robust metric is the pixel deviation since it assumes the colour for pixel  $\bar{\mathbf{u}}_0$  of the central view is correct and quantifies the difference in colour between all other samples of the 4D-PPI and the sample for the reference view:

$$\bar{J}_{PD} = \frac{1}{KL} \sum_{\mathbf{k} \in \mathcal{A}} |\mathbf{I}_{\theta, \bar{\mathbf{u}}_0}(\mathbf{k}) - \mathbf{I}_{\theta, \bar{\mathbf{u}}_0}(\mathbf{k}_r)|, \quad (14)$$

where  $K$  and  $L$  are the number of discrete views of the light field in the horizontal and vertical directions, respectively,  $\mathcal{A}$  is the set of all views of the discrete 4D light field, and  $|\cdot|$  is the element-wise norm operator, such that for  $\mathbf{v} = [v_0 \ \dots \ v_i]^T$ ,  $|\mathbf{v}| = [|v_0| \ \dots \ |v_i|]^T$ . Considering  $\bar{J}_{PD} = [J_{PD}^R \ J_{PD}^G \ J_{PD}^B]^T$ , the scalar cost is defined as the average of the cost of the three colour channels, that is:

$$J_{PD} = \frac{1}{3} (J_{PD}^R + J_{PD}^G + J_{PD}^B). \quad (15)$$

As such, depth values and thus orientations  $\theta$  that obtain the minimum cost should indicate a 4D-PPI with the least changes in colour and, thus, the most photometrically consistent 4D-PPP.

### C. Known Limitations of the 4D-PPP in Depth Estimation

Approaches based solely on photometric consistency, such as the one based in the cost described by Eq. (14), can be highly accurate for a large percentage of situations. However,

such approaches have known limitations that require depth estimation algorithms to explicitly or implicitly base their results on different heuristics and more complex models. This subsection describes some of the photometric consistency-based algorithms' most important known limitations.

1) *Low Variance in the Imaged Texture*: 4D-PPIs with the correct orientation will have near-constant colour outside occlusion and non-Lambertian situations. One way to take advantage of the photometric consistency principle in these cases is to search for the orientation in Eq. (7) that provides a 4D-PPI with near-constant colour. To this end, it is useful to understand what happens when the plane's orientation represented by a given 4D-PPI does not correspond to the correct depth of the 3D-space point imaged by the central view.

Let us assume a 4D Point-Projection Image obtained for a plane intersecting the reference view at a pixel with integer coordinates  $\bar{\mathbf{u}}_0 = \mathbf{m}_0$  with a deviation from the correct angle  $\theta_c$  embodied in a shift  $\delta$ . From Eq. (13), it is:

$$\begin{aligned} \mathbf{I}_{\theta, \mathbf{m}_0}(\mathbf{k}) &= \bar{\mathbf{L}}(\boldsymbol{\eta} \odot (\mathbf{k} - \mathbf{k}_r)) (\tan \theta_c + \delta) + \mathbf{m}_0, \mathbf{k} \\ &= \mathbf{I}_{\theta_c, \mathbf{m}_0 + \delta \boldsymbol{\eta} \odot (\mathbf{k} - \mathbf{k}_r)}(\mathbf{k}) = \mathbf{I}_{\theta, \mathbf{m}'_0}(\mathbf{k}). \end{aligned} \quad (16)$$

The above equation means that when the estimation of the orientation of the plane corresponding to a 3D-space point, and thus its depth, is not correct, the corresponding 4D-PPI  $\mathbf{I}_{\theta, \mathbf{m}_0}(\mathbf{k})$  is equivalent to a 4D-PPI of 3D points that have the correct depth, as given by  $\theta_c$ , but have positions  $\mathbf{m}'_0(\mathbf{k})$ , that depend on the view  $\mathbf{k}$  of the light field.

This points to an important limitation of photometric consistency: if the presented scene had a more homogeneous texture, the images of the 3D-space points associated with the positions  $\mathbf{m}'_0(\mathbf{k})$  could reveal photometric consistency even with an erroneous orientation. This not only limits the types of scenes for which one can obtain accurate samples using such photometric consistency, but it also imposes precision limits to such approaches since, for a small enough error  $\delta$ , the changes in the 4D-PPI may be negligible.

2) *Occlusions*: not all real-world points are visible across all views of the light field. If a given region has in its neighbourhood a second region closer to the camera, the first will become partially occluded as the viewpoint changes. This means that if a 4D-PPP with the correct orientation is chosen for any given point in the occluded region, this plane will *intersect* the plane corresponding to a point from the occluding region.

For instance, let there be two 3D-space points  $\mathbf{x}_0$  and  $\mathbf{x}_{occ}$ , described in the light field by the 4D-PPIs  $\mathbf{I}_{\theta, \mathbf{m}_0}(\mathbf{k})$  and  $\mathbf{I}_{\theta_{occ}, \bar{\mathbf{u}}}(\mathbf{k})$ , respectively. If  $\mathbf{x}_{occ}$  occludes  $\mathbf{x}_0$  then the depth  $z_{occ}$  of  $\mathbf{x}_{occ}$  is necessarily smaller than the depth  $z_0$  of  $\mathbf{x}_0$ . From Eq. (7) this implies that

$$\begin{cases} \theta_{occ} < \theta_0 & \text{if } D > 0, \\ \theta_{occ} > \theta_0 & \text{if } D < 0. \end{cases} \quad (17)$$

In this text, without loss of generality, it can be assumed that  $D < 0$ , meaning the camera centres are located between the sensor and the object. In addition, Eq. (11) implies that  $\mathbf{x}_{occ}$  occludes  $\mathbf{x}_0$  for a given view  $\bar{\mathbf{s}}$  if, and only if, the 4D-PPPs that

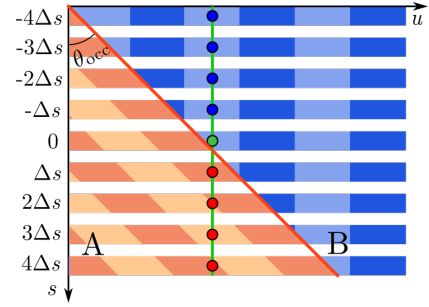


Figure 2: A diagram of an  $s \times u$  EPI segment showcasing two different regions of constant depth. Region A has an orientation  $\theta_{occ}$  and occludes region B, which has orientation  $\theta_0 = 0$ . The green line represents the intersection of the EPI with the 4D-PPP crossing the central view at the point in green  $(m_0\Delta u, 0)$ . Blue circles represent unoccluded samples of the 4D-PPP. Red circles represent its occluded samples.

represent these points intersect at  $\bar{\mathbf{s}}$ . From Equation (11), such an intersection can be described by the following equation:

$$\boldsymbol{\eta} \odot (\bar{\mathbf{s}} - \mathbf{k}_r) \tan \theta_0 + \mathbf{m}_0 = \boldsymbol{\eta} \odot (\bar{\mathbf{s}} - \mathbf{k}_r) \tan \theta_{occ} + \bar{\mathbf{u}}_0. \quad (18)$$

Figure 2 illustrates this situation in an  $s \times u$  EPI. It represents a hypothetical situation with two regions of constant depth and with some texture. Region A represents an occluding region with a constant 4D-PPP angle equal to  $\theta_{occ}$  while region B is a partially occluded region with a 4D-PPP angle  $\theta_0 = 0$ .

The green point represents a light field position  $\mathbf{p}$  for which the orientation  $\theta$  is being estimated. If one supposes that  $\theta(\mathbf{p}) = \theta_0 = 0$ , that is the correct angle for Region B, the 4D-PPP (whose intersection with the EPI is represented as a green line) will intersect both Regions A and B. The samples for views with  $s \geq 0$  will correspond to the occluding region, and the ones for  $s < 0$  will correspond to the occluded region. This implies that the 4D-PPI corresponding to the correct 4D-PPP orientation does not present photometric consistency. Therefore, any method solely based on photometric consistency may lead to inaccurate results in occlusion regions.

3) *Inconsistencies in Surface Reconstruction*: when estimating the depths of a scene by determining the angles  $\theta$  of the 4D Point Projection Planes corresponding to each 3D-space point, the relative positions of neighbouring 3D-space points are not considered. As such, errors in the estimation of the depths of the 3D-space points (e.g., the inaccuracies due to noise) may lead to inconsistencies in the reconstruction of surfaces, such as smooth surfaces appearing rugged or staircase effects in slanted planes. These inconsistencies are evident when estimating surface normals from the 3D reconstruction.

The simplest algorithm for obtaining a surface normal requires an accurate estimation of the 3D coordinates of a 3D-space point  $\mathbf{x}(\mathbf{m}) = [x(\mathbf{m}) \ y(\mathbf{m}) \ z(\mathbf{m})]^T$ , corresponding to pixel coordinates  $\mathbf{m}$  at a given view and two of its neighbours,  $\mathbf{x}(\mathbf{m} + \mathbf{e}_h)$  and  $\mathbf{x}(\mathbf{m} + \mathbf{e}_v)$ , where

$$\mathbf{e}_h = [1 \ 0]^T \quad \text{and} \quad \mathbf{e}_v = [0 \ 1]^T. \quad (19)$$

One can then compute the normal of the surface containing  $\mathbf{x}(\mathbf{m})$ ,  $\mathbf{x}(\mathbf{m} + \mathbf{e}_h)$  and  $\mathbf{x}(\mathbf{m} + \mathbf{e}_v)$  through the cross product:

$$\mathbf{v}(\mathbf{m}) = \boldsymbol{\tau}_h(\mathbf{m}) \times \boldsymbol{\tau}_v(\mathbf{m}), \quad (20)$$

where

$$\begin{aligned} \boldsymbol{\tau}_h(\mathbf{m}) &= \mathbf{x}(\mathbf{m} + \mathbf{e}_h) - \mathbf{x}(\mathbf{m}), \\ \boldsymbol{\tau}_v(\mathbf{m}) &= \mathbf{x}(\mathbf{m} + \mathbf{e}_v) - \mathbf{x}(\mathbf{m}). \end{aligned} \quad (21)$$

However, using only three samples to estimate surfaces may lead to significant errors in the estimation if there are errors in the reconstruction of 3D-space points. For this reason, surface normal maps are often estimated using difference kernel filters [41], that perform smoothing of the 3D-space points before computing  $\boldsymbol{\tau}_h$  and  $\boldsymbol{\tau}_v$ . In this case,  $\boldsymbol{\tau}_h$  and  $\boldsymbol{\tau}_v$  are estimated as:

$$\begin{aligned} \boldsymbol{\tau}_h(\mathbf{m}) &= \sum_{\mathbf{i} \in \mathcal{W}} \mathbf{x}(\mathbf{m} + \mathbf{i}) g_h(\mathbf{i}), \\ \boldsymbol{\tau}_v(\mathbf{m}) &= \sum_{\mathbf{i} \in \mathcal{W}} \mathbf{x}(\mathbf{m} + \mathbf{i}) g_v(\mathbf{i}), \end{aligned} \quad (22)$$

where  $\mathbf{i} \in \mathcal{W} \subset \mathbb{Z}^2$  is the index of a difference kernel filter and  $g_h(\mathbf{i})$  and  $g_v(\mathbf{i})$  are the coefficients of difference kernel filters along the horizontal and vertical directions inside a view, respectively. Usually, if  $\mathbf{i} = [i \ j]$  and  $\mathbf{i}' = [j \ i]$ , then  $g_h(\mathbf{i}) = g_v(\mathbf{i}')$ . While this method improves robustness for large kernel filters, it involves a compromise between the support of the filter and performance around image edges and smaller details of the scene.

The *4D Lightfield Benchmark* [14] proposes the MAE metric to measure surface normal accuracy. This measure consists of the median of the angle differences, in degrees, between the surface normals estimated from a given depth map and a provided ground truth. These normals are estimated with  $g_h(\mathbf{i})$  and  $g_v(\mathbf{i})$  being Scharr filters defined over a  $3 \times 3$  window  $\mathcal{W}$ .

4) *Non-Lambertian scenes*: The light field camera model used in this work and all its equations assume diffuse lighting. Therefore, the concept of 4D-PPPs with photometric consistency does not hold in non-Lambertian scenes, e.g., with reflections or specular lighting, since in these cases, each light ray emitted by a 3D-space point may have a different colour.

Non-Lambertian light field analysis falls outside this article's scope, however, some approaches have been proposed attempting to estimate disparity in non-Lambertian regions. Gutsche *et al.* [42] proposed a way to obtain surface normals in the specular areas, Lee *et al.* [22] proposed a complex-valued measure that takes into account specular regions, and Cui *et al.* [43] proposed an adaptive cross operator, which improves disparity estimation in reflective surfaces.

The remainder of this paper describes a novel algorithm for depth estimation that enforces smoothness in the orientation map, explicitly addressing occlusions and inconsistencies in surface reconstruction while implicitly addressing low-variance textures.

#### IV. ITERATIVE OCCLUSION AWARE DEPTH REFINEMENT

This section presents the Iterative Occlusion Aware Depth Refinement (IOADR) algorithm, which determines the depth

of the 3D-space point associated with each position  $\mathbf{m}$  within a reference view  $\mathbf{k}_r$ . Using the framework defined in Section III, computing such depth is equivalent to obtaining the 4D-PPP orientation map  $\theta(\mathbf{m}, \mathbf{k}_r)$  for  $[\mathbf{m} \ \mathbf{k}_r]$ , as defined by Eq. (9). As pointed out in Subsection III-C, such computation should take into consideration the following factors:

- photometric consistency of the 4D-PPI defined in Subsection III-B;
- occlusions;
- low variance in the imaged texture;
- inconsistencies in surface reconstruction.

This is achieved using a 4D geometry-based cost model considering all these factors when comparing a series of candidate orientations computed from geometric considerations. Thus, the problem of finding the correct 4D-PPP orientation map  $\theta(\mathbf{m}, \mathbf{k}_r)$  is reduced to a cost minimisation problem.

##### A. Architecture and Walkthrough

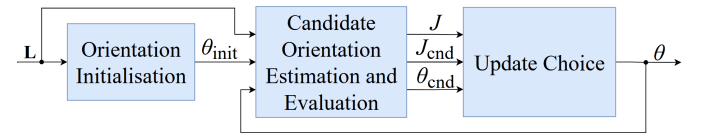


Figure 3: Diagram of the IOADR:  $\mathbf{L}$  represents the light field;  $\theta_{\text{init}}$  represents the initial orientation map;  $\theta$  represents the current working 4D-PPP orientation map and  $J$  its cost;  $\theta_{\text{end}}$  represents the best candidate orientation and  $J_{\text{end}}$  its cost.

The proposed IOADR algorithm iteratively refines an initial orientation estimate through a cost model minimisation strategy. The architecture of the algorithm can be summarised in three major modules, shown in Figure 3, and described as:

- *Orientation Initialisation* — This module provides a fast initialisation of the orientation map  $\theta(\mathbf{m}, \mathbf{k}_r)$  using the structure-tensor [36] on the EPIs of the light field. More details are provided in Subsection IV-B.
- *Candidate Orientation Estimation and Evaluation* — For each sample of the reference view of the light field, given its current orientation  $\theta$ , this module computes a series of candidate orientations based on a random perturbation and three different heuristics: Smooth Orientation, Colour-Orientation Congruence, and Congruent Plane Geometry. The different candidate orientations are then evaluated according to the proposed cost model, and the best one is chosen, with its corresponding cost computed. More details are provided in Subsection IV-C.
- *Update Choice* — Finally, a stochastic decision inspired by the simulated-annealing algorithm [44] is made: the current orientation map is either kept or updated with the best candidate orientation. This increases robustness in the optimisation, preventing the algorithm from getting stuck in a local minima. Further details are provided in Subsection IV-D.

The IOADR algorithm continuously iterates the modules *Candidate Orientation Estimation and Evaluation* and *Update Choice*, with each refinement iteration  $q$  further improving the

orientation map  $\theta^{(q)}(\mathbf{m}, \mathbf{k}_r)$  according to the cost model. Note that for each pixel  $\mathbf{m}$  of the reference view  $\mathbf{k}_r$ , these two modules are run in sequence to generate the orientation map of each iteration  $q$ . Moreover, for even-numbered refinement iterations  $q$ , this iteration over  $\mathbf{m}$  occurs in raster scan order, from left to right and top to bottom, and, for odd-numbered refinement iterations  $q$ , in reverse raster scan order, from right to left and from bottom to top.

### B. Orientation Initialisation

A proper initial orientation map  $\theta^{(0)}(\mathbf{m}, \mathbf{k}_r)$  is required for the IOADR algorithm to converge to an optimal angle map in a reasonable number of iterations. Ideally, it should be obtained by a low-complexity method.

In this regard, gradient-based approaches are good options, providing significant accuracy in non-occluded and non-flat regions with low computational complexity [16]. A straightforward implementation of structure-tensor-based depth estimation proved sufficiently accurate for obtaining an initial orientation map for the IOADR algorithm.

The structure tensor is calculated separately for each colour channel, using the horizontal and vertical EPIs of the light field, resulting in six different orientation maps. The initial 4D-PPP orientation map  $\theta^{(0)}(\mathbf{m}, \mathbf{k}_r)$  is obtained by choosing, for each pixel, the  $\theta$  value from the colour channel  $c$  and EPI direction with the highest structure tensor reliability measure, calculated as in [36].

### C. Candidate Orientation Estimation and Evaluation

To improve the initial orientation map  $\theta^{(0)}(\mathbf{m}, \mathbf{k}_r)$ , the following steps are followed:

- Step 1: estimate, for each pixel  $\mathbf{m}$ , a set of candidate orientations.
- Step 2: evaluate the cost of each of these candidate orientations.
- Step 3: choose the best candidate orientation.

This process's success depends directly on the cost model and the choice of heuristics used to estimate the candidate orientations.

1) *Cost Model*: a novel cost model is proposed, described by function  $J(\theta, \mathbf{p}, q)$ . It is a function of a light field position  $\mathbf{p} = [\mathbf{m} \ \mathbf{k}_r]$ , a candidate orientation  $\theta$  and the algorithm iteration  $q$ , that is defined as follows:

$$J(\theta, \mathbf{p}, q) = J_{dc}(\theta, \mathbf{p}) + \lambda(q)J_{coc}(\theta, \mathbf{p}) + \gamma(q)J_{pg}(\theta, \mathbf{p}), \quad (23)$$

where:

- (a)  $J_{dc}(\theta, \mathbf{p})$  is a 4D Occlusion Aware Data Cost;
- (b)  $J_{coc}(\theta, \mathbf{p})$  is a A Colour-Orientation Congruence Cost;
- (c)  $J_{pg}(\theta, \mathbf{p})$  is a Planar Geometry Cost.

Note that the importance of these terms should not be equal for all iterations  $q$ . For the first iteration, the model is entirely based on the initial disparity map and, as such, presents many problems common to structure-tensor-based maps, namely noisy orientation maps, high density of artefacts, and inaccurate boundaries of foreground objects. Thus, it has been found empirically for all tested light fields that for  $q < 2$ ,

$\lambda(q) = 0$ , that is, the Colour-Orientation Congruence Cost should not be considered. In addition, since the estimation of surface normals requires a rather precise orientation estimate, then for  $q < 4$ ,  $\gamma(q) = 0$ , that is, the Planar Geometry Cost should not be considered. For  $q \geq 2$ ,  $\lambda(q) = \lambda_0$  while for  $q \geq 4$ ,  $\gamma(q) = \gamma_0$  where both  $\lambda_0$  and  $\gamma_0$  are empirically verified parameters of the algorithm. In the sequel, the costs in Eq. (23) are detailed.

a) *4D Occlusion Aware Data Cost*: as addressed in Section III-C, occlusions constitute some of the main difficulties in obtaining accurate 4D-PPP orientation estimates from data costs, such as the variance or the pixel deviation of potential 4D-PPIs. This section introduces a data cost that addresses this problem explicitly.

The proposed 4D Occlusion-Aware Data Cost  $J_{dc}(\theta_0, \mathbf{p}_0)$  evaluates a given orientation  $\theta_0$  by estimating the pixel deviation, described in Eqs. (14) and (15), of the *unoccluded* views of the 4D-PPP with orientation  $\theta_0$ , and associated with a given position  $\mathbf{p}_0 = [\mathbf{m}_0^T \ \mathbf{k}_r^T]^T$  of the light field.

Algorithm 1 below describes the process of calculating  $J_{dc}(\theta_0, \mathbf{p}_0)$  in full.

---

#### Algorithm 1 - 4D Occlusion-Aware Data Cost

---

##### I. Inputs:

- The discrete light field  $\mathbf{L}(\mathbf{p})$ .
- The maximum orientation of the light field  $\theta_{\max}$ , associated with the minimum depth of the scene.
- The current orientation map  $\theta(\mathbf{m}, \mathbf{k}_r)$ .
- The current light field position  $\mathbf{p}_0 = [\mathbf{m}_0^T \ \mathbf{k}_r^T]^T$ .
- The candidate orientation  $\theta_0$  for the current 4D-PPP.

##### II. Outputs:

- 4D Occlusion-Aware Data Cost  $J_{dc}(\theta_0, \mathbf{p}_0)$

##### III. Initialisation:

- i. Compute  $\bar{\theta}(\bar{\mathbf{u}}, \mathbf{k}_r)$  by bi-linearly interpolating [39]  $\theta(\mathbf{m}_0, \mathbf{k}_r)$ .
- ii. From Eq. (18), as  $\theta_0 < \theta_{occ} < \theta_{\max}$  and  $\Delta_o = \|\mathbf{m}_0 - \bar{\mathbf{u}}_0\|_\infty$  is maximum when  $\bar{\mathbf{s}} = \mathbf{k}_{\max}$ , the corner view of the light field that has maximum  $L_\infty$  distance to  $\mathbf{k}_r$ , find the maximum distance  $\Delta_{o\max}$ :

$$\Delta_{o\max} = (\tan \theta_{\max} - \tan \theta_0) \|\boldsymbol{\eta} \odot (\mathbf{k}_{\max} - \mathbf{k}_r)\|_\infty, \quad (24)$$

where  $\|\mathbf{v}\|_\infty = \max_i |v_i|$ .

- iii. Determine the set  $\mathcal{T}$  of the  $\theta$  parameters of all 4D-PPP that can possibly occlude the current 4D-PPP:

$$\mathcal{T} = \left\{ \theta(\mathbf{m}, \mathbf{k}_r) \mid \|\mathbf{m} - \mathbf{m}_0\|_\infty \leq \Delta_{o\max} \wedge \theta(\mathbf{m}, \mathbf{k}_r) > \theta_0 \right\}. \quad (25)$$

##### IV. Data Cost Calculation

- i. From Eq. (18), determine, for each view  $\mathbf{k}$  of the light field and for each  $\theta_{occ} \in \mathcal{T}$ :
  - i) The parameter  $\bar{\mathbf{u}}_0 = \bar{\mathbf{u}}_{occ}$  of a hypothetical 4D-PPP with orientation  $\theta_{occ}$  intersecting the current 4D-PPP at  $\mathbf{k}$  as:

$$\bar{\mathbf{u}}_{occ} = \boldsymbol{\eta} \odot (\mathbf{k} - \mathbf{k}_r) (\tan \theta_{occ} - \tan \theta_0) + \mathbf{m}_0, \quad (26)$$

- ii) The coordinates  $\bar{\mathbf{s}}$  where a 4D-PPP with parameters  $\bar{\mathbf{u}}_0 = \bar{\mathbf{u}}_{\text{occ}}$  and  $\theta = \bar{\theta}(\bar{\mathbf{u}}_{\text{occ}}, \mathbf{k}_r)$  intersects the current 4D-PPP.
- iii. For all  $\bar{\mathbf{s}}$  computed above, determine the set  $\mathcal{U}$ , with cardinality  $|\mathcal{U}|$ , of unoccluded views  $\mathbf{k}$  of the 4D-PPP as

$$\mathcal{U} = \left\{ \mathbf{k} \mid \|\mathbf{k} - \bar{\mathbf{s}}\|_\infty < \tau_{\text{occ}} \right\}, \quad (27)$$

where  $\tau_{\text{occ}} = \frac{1}{2}$ .

- iii. Compute  $\bar{\mathbf{J}}_{\text{oapd}}(\theta_0, \mathbf{p}_0) = [J_{\text{oapd}}^{\text{R}} \ J_{\text{oapd}}^{\text{G}} \ J_{\text{oapd}}^{\text{B}}]$ , the Occlusion Aware Pixel Deviation (OAPD) for each colour channel, as:

$$\bar{\mathbf{J}}_{\text{oapd}}(\theta_0, \mathbf{p}_0) = \frac{1}{|\mathcal{U}|} \sum_{\mathbf{k} \in \mathcal{U}} |(\mathbf{I}_{\theta, \mathbf{m}_0}(\mathbf{k}) - \mathbf{I}_{\theta, \mathbf{m}_0}(k_r, l_r))|. \quad (28)$$

- iv. Compute a scalar cost  $J_{\text{oapd}}(\theta_0, \mathbf{p}_0)$  as the average of each colour channel, that is:

$$J_{\text{oapd}}(\theta_0, \mathbf{p}_0) = \frac{1}{3} (J_{\text{oapd}}^{\text{R}} + J_{\text{oapd}}^{\text{G}} + J_{\text{oapd}}^{\text{B}}). \quad (29)$$

- v. Compute  $J_{\text{pd}}(\theta_0, \mathbf{p}_0)$  according to Eqs. (14) and (15).
- vi. If  $|\mathcal{U}|$  is smaller than 5% of the number of views of the light field, then

$$J_{\text{dc}}(\theta_0, \mathbf{p}_0) = J_{\text{pd}}(\theta_0, \mathbf{p}_0), \quad (30)$$

else

$$J_{\text{dc}}(\theta_0, \mathbf{p}_0) = \min\{J_{\text{pd}}(\theta_0, \mathbf{p}_0), J_{\text{oapd}}(\theta_0, \mathbf{p}_0)\}. \quad (31)$$

---

### End of Algorithm 1

---

*b) Colour-Orientation Congruence Cost:* In general, if samples of the light field that are close have a similar colour, then their corresponding 3D-space points tend to have a similar depth. Thus, their corresponding 4D-PPPs tend to have similar orientations  $\theta$  (Eq. (7)). This occurs because an abrupt change in depth indicates an occlusion—a transition between objects, which often implies some colour change.

The proposed algorithm introduces a Colour-Orientation Congruence term to the data cost. This term is based on the smoothness cost from Schilling *et al.* [24], which is a good fit for the proposed algorithm as it is sufficiently robust and takes full advantage of the access to an estimate of neighbouring angles  $\theta$  that the proposed algorithm provides.

Given a candidate orientation  $\theta$ , the Colour-Orientation Congruence term  $J_{\text{coc}}$  is computed at the light field position  $\mathbf{p} = [\mathbf{m} \ \mathbf{k}_r]^T$  as:

$$J_{\text{coc}}(\theta, \mathbf{m}, \mathbf{k}_r) = (\tan \theta - \tan(\theta_{\text{sea}}(\mathbf{m}, \mathbf{k}_r)))^2, \quad (32)$$

where  $\theta_{\text{sea}}(\mathbf{m}, \mathbf{k}_r)$  is a smoothed edge-aware version of  $\theta(\mathbf{m}, \mathbf{k}_r)$  that tries to preserve edges in  $\theta(\mathbf{m}, \mathbf{k}_r)$ , and also is aware of edges in the corresponding colour. It is obtained as:

$$\theta_{\text{sea}}(\mathbf{m}, \mathbf{k}_r) = \tan^{-1} \left( \frac{\sum_{\mathbf{m}_0 \in \mathcal{W}^c} \chi(\mathbf{m}_0) \theta(\mathbf{m}_0, \mathbf{k}_r)}{\sum_{\mathbf{m}_0 \in \mathcal{W}^c} \chi(\mathbf{m}_0)} \right), \quad (33)$$

where  $\chi(\mathbf{m}_0)$  is the weight of the orientation sample at  $\mathbf{m}_0$  and  $\mathcal{W}^c$  is a window around position  $\mathbf{m}$  in the reference view  $\mathbf{k}_r$ . In order to compute  $\chi(\mathbf{m}_0)$ , one starts by computing an orientation difference  $\Delta_\theta(\mathbf{m}_0)$  and a colour difference  $\Delta_c(\mathbf{m}_0)$  as

$$\Delta_\theta(\mathbf{m}_0) = \rho_\theta |\tan \theta(\mathbf{m}_0, \mathbf{k}_r) - \tan \theta|, \quad (34)$$

$$\Delta_c(\mathbf{m}_0) = \rho_c \|\mathbf{L}(\mathbf{m}_0, \mathbf{k}_r) - \mathbf{L}(\mathbf{m}, \mathbf{k}_r)\|, \quad (35)$$

where  $\rho_\theta$  and  $\rho_c$  are the relative weights of these differences, defined empirically. Then the weight of the orientation sample  $\chi(\mathbf{m}_0)$  can be computed as

$$\chi(\mathbf{m}_0) = \max \left\{ \epsilon_\theta, \sqrt{\Delta_\theta(\mathbf{m}_0)^2 + \Delta_c(\mathbf{m}_0) \Delta_\theta(\mathbf{m}_0)} \right\}^{-1}, \quad (36)$$

for  $\Delta_c(\mathbf{m}_0) \leq \tau_c$  and  $\Delta_\theta(\mathbf{m}_0) \leq \tau_o$ , and

$$\chi(\mathbf{m}_0) = \max \left\{ \epsilon_\theta, \sqrt{\Delta_c(\mathbf{m}_0)^2 + \Delta_\theta(\mathbf{m}_0)^2} \right\}^{-1}, \quad (37)$$

for  $\Delta_c(\mathbf{m}_0) \leq \tau_c$  and  $\Delta_\theta(\mathbf{m}_0) > \tau_o$ , where  $\epsilon_\theta$  and  $\tau_c$  are determined empirically and  $\tau_o$  is the dynamic range of  $\tan \theta$  for the light field being processed. In all other cases,  $\chi(\mathbf{m}_0)$  is set to zero.

A small cost, therefore, implies that the candidate  $\theta$  is congruent with the light field colour variations. In contrast, a high cost implies that the candidate  $\theta$  would lead to abrupt transitions in the orientation map that are not matched by the expected colour variation in the light field.

*c) Planar Geometry Cost:* As discussed in Section III-C, using only the Data Cost  $J_{\text{dc}}$  (Eq. (31)) and the Colour-Orientation Congruence cost  $J_{\text{coc}}$  (Eq. (32)), it is possible that errors in the orientation map estimation lead to 3D reconstructions that render planar surfaces with a rugged appearance or stair-case effects.

To mitigate this issue, the introduction of a novel planar geometry cost  $J_{\text{pg}}(\theta, \mathbf{m}, \mathbf{k}_r)$  term to the data cost is proposed. This planar geometry cost term is based on the fact that if the 4D-PPP orientations are correct, then the depths of the corresponding 3D-space points, and thus their 3D locations  $\mathbf{x}_c(\mathbf{m}, \mathbf{k}_r)$ , are correct. Therefore, the estimation of surface normals using just simple differences, as in Eq. (21), should yield the same results as employing a smoother estimate, such as the one obtained with a larger kernel, in Eq. (6). A large difference between these two estimates can imply two things: the region of interest is not planar, or the values of  $\mathbf{x}_c(\mathbf{m}, \mathbf{k}_r)$  used in the simpler surface normal estimate, and thus the corresponding 4D-PPP orientations, are not correct.

The algorithm to estimate the Planar Geometry Cost is included in the Candidate Orientation Estimation and Evaluation Module in Figure 3 which means the algorithm runs in sequence with the Update Choice Module for each sample  $\mathbf{m}$  of the reference view  $\mathbf{k}_r$  to generate a refined sample of the current orientation map  $\theta(\mathbf{m}, \mathbf{k}_r)$ . As described in Subsection IV-A, the raster scan order of iteration over  $\mathbf{m}$  depends on the parity of  $q$ . As such, for each iteration  $q$ , a smooth surface normal map,  $\mathbf{v}(\mathbf{m}, \mathbf{k}_r)$ , is computed using only the orientation map  $\theta(\mathbf{m}, \mathbf{k}_r)$  samples already refined in iteration  $q$ . The proposed Planar Geometry Cost computation is described below in Algorithm 2.



---

**Algorithm 2 - Planar Geometry Cost**


---

**I. Inputs:**

- Orientation Candidate  $\theta_0$ .
- Current Position  $\mathbf{m}_0$  in the reference view.
- Current Orientation Map  $\theta(\mathbf{m}, \mathbf{k}_r)$ .
- Current refinement iteration  $q$ .
- Current Surface Normal Map  $\mathbf{v}(\mathbf{m}, \mathbf{k}_r)$
- Support  $(2\delta_a + 1) \times (2\delta_a + 1)$  of the estimation filters, where  $\delta_a \in \mathbb{N}$ .

**II. Outputs:**

- Planar Geometry Cost  $J_{\text{pg}}(\theta_0, \mathbf{m}_0, \mathbf{k}_r)$

**III. Initialisation:**

- i. The 3D-space candidate position  $\mathbf{x}_0$  and the 3D-space point map  $\mathbf{x}(\mathbf{m}, \mathbf{k}_r)$  are obtained, respectively, from  $\theta_0$  and  $\theta(\mathbf{m}, \mathbf{k}_r)$ , using Eqs. (6) and (11).
- ii. The Gaussian kernel is set as

$$g_G(i, j) = ie^{-\frac{i^2 + j^2}{(2\delta_a + 1)^2}}, -\delta_a \leq i, j \leq \delta_a,$$

and the difference kernel is set as

$$g_D(i, j) = \begin{cases} 0, & \text{if } |j| > 0 \wedge |i| > 1, \\ i, & \text{otherwise.} \end{cases}$$

- iii. To evaluate the normal for the current sample, the difference filter must be offset. Therefore, to account for samples that have been refined in the current iteration, we have:

$$\begin{aligned} g_{\text{evl}}^h(\mathbf{i}) &= g_D(i + 1, j) \text{ when } q \text{ is even,} \\ g_{\text{evl}}^h(\mathbf{i}) &= g_D(i - 1, j) \text{ when } q \text{ is odd,} \\ \text{and } g_{\text{evl}}^v(i, j) &= g_{\text{evl}}^h(j, i), \forall i, j. \end{aligned}$$

**IV. Planar Geometry Cost Calculation**

- i. Update sample  $\mathbf{v}(\mathbf{m}_0, \mathbf{k}_r)$  of the estimated normal map using Eqs. (20) to (22) using the gaussian Kernel  $g_D$  as the difference filter.
- ii. Obtain all samples  $\mathbf{v}(\mathbf{m}_j, \mathbf{k}_r)$ , with  $\mathbf{m}_j$  inside a window  $\mathcal{W}^a$  centred in  $\mathbf{m}_0$ .
- iii. Compute the set  $\mathcal{S}$  of all samples  $\mathbf{m}_j$  for which the angles between  $\mathbf{v}(\mathbf{m}_0, \mathbf{k}_r)$  and  $\mathbf{v}(\mathbf{m}_j, \mathbf{k}_r)$ , the samples of the estimated normal map, are below the average of the angles corresponding to set  $\mathcal{W}^a$  weighed by an empirically defined parameter  $\tau_a$ :

$$\mathcal{S} = \{\mathbf{m}_j \mid \cos^{-1}\langle \mathbf{v}(\mathbf{m}_0, \mathbf{k}_r), \mathbf{v}(\mathbf{m}_j, \mathbf{k}_r) \rangle < \tau_a \mu\}, \quad (38)$$

where

$$\mu = \frac{1}{|\mathcal{W}^a|} \sum_{\mathbf{m}_j \in \mathcal{W}^a} \cos^{-1}\langle \mathbf{v}(\mathbf{m}_0, \mathbf{k}_r), \mathbf{v}(\mathbf{m}_j, \mathbf{k}_r) \rangle. \quad (39)$$

- iv. Be  $\mathbf{v}_\mu$  the average  $\frac{1}{|\mathcal{S}|} \sum_{\mathbf{m}_j \in \mathcal{S}} \mathbf{v}(\mathbf{m}_j, \mathbf{k}_r)$  normalised to unit norm, and, for all  $\mathbf{m}_j \in \mathcal{S}$ , compute  $z(\mathbf{m}_0, \mathbf{m}_j)$  such that:

$$z(\mathbf{m}, \mathbf{m}_j) = \frac{\langle \mathbf{v}_\mu, \mathbf{x}(\mathbf{m}_j, \mathbf{k}_r) \rangle}{\langle \mathbf{v}(\mathbf{m}_j, \mathbf{k}_r), [\Delta u \ \Delta v \ 1]^T \odot \mathbf{m}_0 \rangle}, \quad (40)$$

where  $\Delta u$  and  $\Delta v$  are the dot pitches in each view.

- v. Compute  $\theta_e(\mathbf{m}_0, \mathbf{m}_j, \mathbf{k}_r)$  from  $z(\mathbf{m}_0, \mathbf{m}_j)$  using Equation (7).

- vi. Compute set  $\mathcal{R}$  of all  $\mathbf{m}_j$  such that:

$$\mathcal{R} = \{\mathbf{m}_j \mid |\tan \theta_e(\mathbf{m}_0, \mathbf{m}_j) - \tan \theta(\mathbf{m}_0, \mathbf{k}_r)| < \tau_\theta\}, \quad (41)$$

where  $\tau_\theta$  is determined empirically.

- vii. Compute  $z_{\text{mu}}(\mathbf{m}_0, \mathbf{m}_j)$  as

$$z_\mu(\mathbf{m}, \mathbf{m}_j) = \frac{\frac{1}{|\mathcal{R}|} \sum_{\mathbf{m}_j \in \mathcal{R}} \langle \mathbf{v}_\mu, \mathbf{x}(\mathbf{m}_j, \mathbf{k}_r) \rangle}{\langle \mathbf{v}_\mu, [\Delta u \ \Delta v \ 1]^T \odot \mathbf{m}_0 \rangle}, \quad (42)$$

- viii. Compute the final orientation estimate  $\theta_\mu$  using Eqs. (42) and (7).

- ix. Being  $\tau_\epsilon$  is an empirical threshold, if  $|\tan \theta_\mu - \tan \theta(\mathbf{m}_0, \mathbf{k}_r)| > \tau_\epsilon$  then

$$J_{\text{pg}}(\theta_0, \mathbf{m}_0, \mathbf{k}_r) = 0,$$

since the region does not represent a plane.

else

- i. Create a  $\mathbf{x}'(\mathbf{m}_0, \mathbf{k}_r)$  such that  $\mathbf{x}'(\mathbf{m}_0, \mathbf{k}_r) = \mathbf{x}_0$ , the 3D-space candidate position, and  $\mathbf{x}'(\mathbf{m}, \mathbf{k}_r) = \mathbf{x}(\mathbf{m}, \mathbf{k}_r)$ ,  $\forall \mathbf{m} \neq \mathbf{m}_0$ .

- ii. Estimate  $\mathbf{v}_{\text{evl}}(\mathbf{m}, \mathbf{k}_r)$ , using Eqs. (20) and (22) with  $\mathbf{x}(\mathbf{m}) = \mathbf{x}'(\mathbf{m}, \mathbf{k}_r)$  and with  $g_h(\mathbf{i}) = g_{\text{evl}}^h(\mathbf{i})$  and  $g_v(\mathbf{i}) = g_{\text{evl}}^v(\mathbf{i})$  and set

$$J_{\text{pg}}(\theta_0, \mathbf{m}_0, \mathbf{k}_r) = \cos^{-1}\langle \mathbf{v}_\mu(\mathbf{m}, \mathbf{k}_r), \mathbf{v}_{\text{evl}}(\mathbf{m}, \mathbf{k}_r) \rangle.$$

---

**End of Algorithm 2**


---

2) *Candidate Orientation Heuristics*: using the scheme in Figure 3, when minimising the cost  $J(\theta, \mathbf{p}, q)$  in Eq. (23), it is helpful to devise heuristics to compute additional candidate orientations  $\theta_{\text{cnd}}(\mathbf{m}, \mathbf{k}_r)$  helping to avoid local minima. Schilling *et al.* in [24] propose using neighbour orientations. However, from the analysis of the proposed model, it is clear that other heuristics can be equally instrumental in finding helpful candidate orientations. In the following, four different heuristics for finding candidate orientations are proposed: Smooth Depth, Colour-Orientation Congruence, Smooth Geometry, and simple Random Perturbation.

a) *Smooth Depth Heuristic Candidate Orientation*: the smooth depth heuristic indicates that the depth found in adjacent pixels should, in most cases, be similar. This heuristic holds outside occlusion regions, so it makes sense to use the  $\theta$  of neighbouring pixels as candidate orientations.

Likewise [24], only the  $\theta$  values of the neighbouring pixels updated in the current iteration  $q$ , are used as candidate orientations.

b) *Colour-Orientation Congruence Heuristic Candidate Orientation*: the Colour-Orientation Congruence cost in Sub-section IV-C1b is designed to promote smoothness in the orientation map when the reference view is smooth in terms of colour. Therefore, one possible heuristic for  $\theta_{\text{cnd}}(\mathbf{m}, \mathbf{k}_r)$  is to make  $\theta_{\text{cnd}}(\mathbf{m}, \mathbf{k}_r) = \theta_{\text{sea}}(\mathbf{m}, \mathbf{k}_r)$  (Eq. (32)).

c) *Smooth Plane Geometry Heuristic Candidate Orientation*: similarly to the case of the Colour-Orientation Congruence Heuristic, another possible simple heuristic for  $\theta_{\text{cnd}}(\mathbf{m}, \mathbf{k}_r)$  is to use  $\theta$  that minimises the planar geometry

cost, that is,  $\theta_{\text{cnd}}(\mathbf{m}, \mathbf{k}_r) = \theta_{\text{avg}}(\mathbf{m}_0)$  (Step IV.vii from Algorithm 2).

As this orientation is derived from a planar assumption it is only used in cases where  $|\theta_{\text{avg}}(\mathbf{m}_0) - \theta(\mathbf{m}_0)| \leq \tau_\epsilon$ , as in Step IV.viii from Algorithm 2.

d) *Random Perturbation Candidate Orientation*: as in the set-up suggested in [24], a random small perturbation of the current 4D-PPP orientation is used as a candidate, allowing the algorithm to slowly move away from a sub-optimal result even when other heuristics fail for a given pixel of the light field. Such  $\theta_{\text{cnd}}(\mathbf{m}, \mathbf{k}_r)$  can be obtained from:

$$\theta_{\text{cnd}}(\mathbf{m}, \mathbf{k}_r) = \tan^{-1}(\tan \theta(\mathbf{m}, \mathbf{k}_r) + \zeta), \quad (43)$$

where  $\zeta$  is sampled from a normal distribution with zero mean. It has been determined empirically that a standard deviation of 0.04 provides a robust compromise for all light fields.

#### D. Update Choice

Finally, the proposed algorithm decides between the current orientation estimate and  $\theta_{\text{cnd}}(\mathbf{m}_0, \mathbf{k}_r)$  through a simulated-annealing-based comparison. For a given iteration  $q$ , if  $\mathbf{p}_0 = [\mathbf{m}_0 \ \mathbf{k}_r]^T$ , a threshold  $\text{Th}$  is computed from the costs obtained from Eq. (23) as:

$$\text{Th} = e^{\frac{J(\theta(\mathbf{p}_0), \mathbf{p}_0, q) - J(\theta_{\text{cnd}}(\mathbf{p}_0), \mathbf{p}, q)}{T^{(q)}}}, \quad (44)$$

where  $T^{(q)}$  is the temperature parameter for the current iteration  $q$ . If  $\text{Th} > 1$  then  $J(\theta_{\text{cnd}}(\mathbf{p}_0), \mathbf{p}_0, q) < J(\theta(\mathbf{p}_0), \mathbf{p}_0, q)$  and the candidate orientation will replace the current estimate. Otherwise, the value  $\text{Th}$  represents the probability of  $\theta_{\text{cnd}}(\mathbf{p}_0)$  being chosen over the current estimate, providing a possibility of choosing  $\theta_{\text{cnd}}(\mathbf{p}_0)$ , even when it incurs a cost that is larger than the one of the current estimate. This decreases the likelihood of the algorithm to converge to local minima [44].

This process is repeated for all pixels of the reference view of the light field over  $N_i$  iterations. The temperature  $T$  is decreased over the iterations according to an exponential multiplicative cooling schedule, as suggested in [45]:

$$T^{(q)} = T_0 \alpha^{\lfloor \frac{N_i}{N_T} \rfloor}, \quad (45)$$

with  $0 < \alpha < 1$ . The initial temperature  $T_0$  and  $\alpha$  are parameters of the algorithm, and it has been verified experimentally that  $T_0 = 10$  and  $\alpha = 0.8$  provide a robust compromise for most light fields.

## V. EXPERIMENTAL RESULTS

This section is divided into three parts. The first describes the experimental conditions. The second presents Ablation Studies, where each of the contributions of the proposed framework is analysed individually, by evaluating the effects of excluding a specific contribution. The third shows a comparison between results achieved with the proposed method and the state-of-the-art.

### A. Experimental Conditions

The IOADR algorithm was implemented in C++ and its source code is available at <https://github.com/RuiLourenco/IOADR>. The algorithm is tested using the HCI 4D Lightfield dataset [14], a computer-generated light field dataset that provides ground truth disparity maps, which allow for objective comparisons. The centre view of each light field and the respective ground truth disparity are shown in Figure 4. Referring to Eq. (12), all light fields in the HCI 4D Lightfield dataset [14] have  $\boldsymbol{\eta} = [\eta \ \eta]$ , and therefore their disparities in the  $s \times u$  and  $t \times v$  directions are the same. All the results presented in this section are relative to these disparities.



Figure 4: Centre views (above) and respective ground truth disparity maps (below) of light fields from the HCI 4D Lightfield Benchmark. From left to right: Boxes, Cotton, Dino, and Sideboard.

Three metrics are employed: two evaluate pixel-wise accuracy – the Mean Squared Error  $\times 100$  and the badpix 0.07; the third one – the Median Angle Error (MAE) in planar regions – evaluates the error in the estimation of surface normals calculated from the disparities (Section III-C), that takes into account sets of neighbouring disparities. This metric is calculated exclusively in planar regions of the light fields using a ground-truth binary map provided by the dataset. These three objective metrics are defined in [14].

All parameters of the IOAOR algorithm were chosen empirically through an automated parameter search, minimising the metrics presented in this section. Table I lists the values used for each parameter.

Table I: Values for different parameters used in the proposed algorithm.  $\eta$  is such that, in Eq. (12),  $\boldsymbol{\eta} = [\eta \ \eta]$ .

Parameter	Value	Parameter	Value	Parameter	Value
$T_0$	10	$\rho_c$	0.15	$\tau_a$	1.3
$N_T$	2	$\rho_\theta$	10	$\delta_a$	5
$N_i$	10	$\tau_c$	3	$\sigma_a$	0.04
$\alpha$	0.8	$\tau_\epsilon$	$\frac{0.031}{\eta}$	$\lambda_0$	100
$\epsilon_\theta$	0.5	$\tau_\theta$	$\frac{0.031}{\eta}$	$\gamma_0$	0.05

### B. Ablation Study

This section assesses the effectiveness of Occlusion Detection, the multi-term energy cost function, and the various

heuristics for estimating candidate orientations  $\theta$ . The baseline is given by the results obtained using the complete proposed data cost in Eq. (23).

1) *Occlusion Awareness*: one of the contributions of this work is the introduction of a 4D occlusion detection algorithm, resulting in the introduction of the Occlusion Aware Pixel Deviation (OAPD), presented in Eq. (29). This is used to formulate the novel data cost  $J_{dc}$  in Eq. (31), which is robust to occlusions. To better evaluate the performance of the proposed contribution, the disparity estimation accuracy using  $J_{dc}$  is compared with the one obtained using the simple Pixel Deviation as in Eq. (15).

Table II: MSE $\times$ 100 and Badpix 0.07 results with and without the occlusion aware data cost  $J_{dc}$ . The best results for each light field are in bold.

Data Cost	Boxes	Cotton	Dino	Sideboard
MSE $\times$ 100				
$J_{pd}$ (Eq. (15))	9.472	4.113	0.832	3.104
$J_{dc}$ (Eq. (31))	<b>4.601</b>	<b>0.375</b>	<b>0.319</b>	<b>0.962</b>
Badpix 0.07				
$J_{pd}$ (Eq. (15))	19.94%	5.28%	5.88%	13.07%
$J_{dc}$ (Eq. (31))	<b>15.53%</b>	<b>2.21%</b>	<b>3.09%</b>	<b>8.01%</b>

Table II shows the Mean Squared Error and Badpix 0.07 results for computer-generated light fields. When compared with the use of the simple Pixel Deviation  $J_{pd}$ , the use of the proposed occlusion aware cost  $J_{dc}$  provides a steep reduction in both metrics for all four tested light fields, achieving a 90% reduction in global MSE for the Cotton light field.

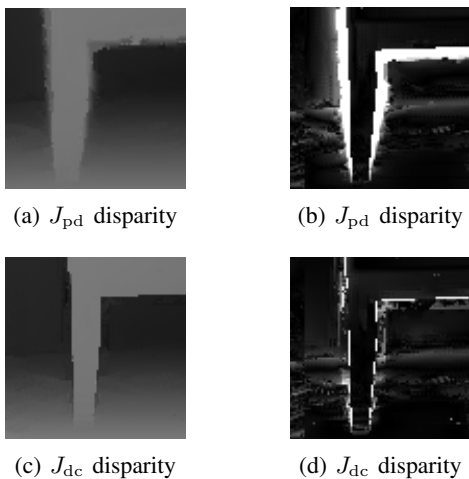


Figure 5: Occlusion details of the disparity map for the light field *Sideboard* using the proposed framework: (a) with the simple Pixel Deviation  $J_{pd}$  in Eq. (15); (b) absolute value of the difference between the disparity in (a) and the ground truth; (c) with the proposed data cost  $J_{dc}$  in Eq. (31); (d) absolute value of the difference between the disparity in (c) and the ground truth.

This is confirmed in Figure 5, which shows a visual comparison of the disparity maps obtained using  $J_{dc}$  and  $J_{pd}$  for the computer-generated light field *Sideboard*. The first row shows

the disparity map obtained from the proposed framework using the simple Pixel Deviation cost  $J_{pd}$  in Eq. (15), and the second row shows the disparities obtained using the proposed data cost  $J_{dc}$  in Eq. (31). The right column shows the absolute differences between the obtained disparities and the ground truth, where white corresponds to the larger error and black corresponds to no error. The borders are far more accurate when the proposed Occlusion-Aware Data Cost  $J_{dc}$  is used, instead of the simple pixel deviation  $J_{pd}$ .

2) *Energy Cost Model*: the three-factor cost model, described in Eq. (23), is another contribution of this work. Therefore, it is important to assess the impact of the inclusion of the Colour-Orientation Congruence cost  $J_{coc}$  and plane geometry cost  $J_{pg}$ . Table III compares the Mean Squared Error, Bad Pix, and MAE when using the full cost in Eq. (23), when using only the data cost  $J_{dc}$ , as well as when excluding only either  $J_{coc}$  or  $J_{pg}$ . As can be seen in Table III, the use of  $J_{coc}$  significantly improves all three metrics. In contrast,  $J_{pg}$  tends to slightly raise the MSE $\times$ 100 and badpix 0.7 metrics, sacrificing some accuracy for heavy improvements in the MAE in planar regions.

Table III: Assessment of MSE $\times$ 100, Badpix 0.07 and MAE for ablation studies excluding some of the different terms of the total energy cost  $J$  in Eq. (23). The best result for each light field is in bold.

Cost Terms (Eq. (23))			Boxes	Cotton	Dino	Sideboard
$J_{pg}$	$J_{coc}$	$J_{dc}$	MSE $\times$ 100			
X	X	X	<b>4.590</b>	<b>0.356</b>	<b>0.312</b>	<b>0.962</b>
		X	5.680	1.202	0.936	1.818
		X	5.490	1.006	0.766	1.717
X	X	X	4.601	0.375	0.319	<b>0.962</b>
$J_{pg}$	$J_{coc}$	$J_{dc}$	Badpix 0.07			
X	X	X	<b>15.27%</b>	<b>1.59%</b>	<b>2.85%</b>	<b>7.86%</b>
		X	34.07%	21.27%	18.26%	22.41%
		X	27.21%	12.07%	11.90%	18.56%
X	X	X	15.53%	2.21%	3.09%	8.01%
$J_{pg}$	$J_{coc}$	$J_{dc}$	MAE in planar regions			
	X	X	6.327	3.651	5.188	8.889
X		X	64.317	82.951	28.962	50.214
		X	52.748	79.040	23.248	47.952
X	X	X	<b>1.819</b>	<b>2.885</b>	<b>0.593</b>	<b>3.706</b>

3) *Candidate Orientations*: a further contribution of this work is the proposal of using multiple different heuristics for finding candidate orientations  $\theta$ , in Subsection IV-C2. This contribution is assessed for MSE $\times$ 100, Badpix 0.07 and MAE in planar regions by excluding the candidates obtained with smooth depth, Colour-Orientation Congruence and smooth plane heuristics.

Table IV shows the results achieved with the proposed algorithm when the candidates are determined foregoing one of the candidate Orientation Heuristics: Smooth Depth, Colour-Orientation Congruence (C-O Congruence), and Smooth Plane heuristics are forgone. On one hand, the significant loss in accuracy obtained from foregoing the smooth depth heuristic and the Smooth Plane Heuristic is worth noticing, both demonstrating significant increases in both MSE $\times$ 100 and Badpix

Table IV: Assessment of MSE×100, Badpix 0.07 and MAE in planar regions when excluding some of the candidate orientation estimation heuristics defined in Section IV-C from the framework. The best result for each light field is in bold.

	Boxes	Cotton	Dino	Sideboard
Excluded Heuristics	MSE × 100			
Smooth Depth	9.401	2.686	0.640	1.566
C-O Congruence	4.692	0.376	0.345	1.004
Smooth Plane	4.768	0.538	0.479	1.128
None	<b>4.601</b>	<b>0.375</b>	<b>0.319</b>	<b>0.962</b>
Excluded Heuristics	Badpix 0.07			
Smooth Depth	24.51%	7.21%	7.79%	13.15%
C-O Congruence	<b>14.77%</b>	<b>2.17%</b>	3.34%	8.24%
Smooth Plane	26.08%	14.71%	14.47%	18.21%
None	15.53%	2.21%	<b>3.09%</b>	<b>8.01%</b>
Excluded Heuristics	MAE in planar regions			
Smooth Depth	2.268	9.253	1.038	4.044
C-O Congruence	2.390	2.913	0.716	4.424
Smooth Plane	56.882	81.628	50.197	56.153
None	<b>1.819</b>	<b>2.885</b>	<b>0.593</b>	<b>3.706</b>

0.07 when excluded. Foregoing the Smooth Plane Heuristic additionally results in a major increase in MAE.

On the other hand, the inclusion of candidate orientations based on Colour-Orientation Congruence has a lesser impact on the accuracy of the resultant disparity map; in fact, not including these candidates even yields minor improvements the Badpix 0.07 metric for some light fields. However, its use leads to a significant improvement in MAE.

### C. Comparison with State-of-the-Art

Table V compares the proposed method with five different state-of-the-art algorithms. Three non-learning based—Ober-Cross [24], Ober-Cross + ANP [24], and OFSY [46]—and two learning-based—EPINet [8] and AttNet [9] in terms of MSE × 100, Badpix 0.07, and MAE in planar regions.

The proposed IOAOR algorithm proves to be superior to all state-of-the-art methods in terms of MAE in Planar Regions, achieving, on average, a 26.3% better result when compared to the second-best method, OFSY [46], which explicitly focuses on the accuracy of surface normals. Yet, the IOAOR algorithm outperforms the OFSY algorithm also in terms of MSE×100 and Badpix 0.07 for all assessed light fields. Regarding pixel-wise accuracy, as measured by MSE×100 and Badpix 0.07, the IOAOR algorithm achieves results competitive with the other state-of-the-art methods, both learning-based and non-learning-based.

## VI. CONCLUSION

This paper introduces a formal mathematical framework for describing depth estimation based on 4D light field geometry. This framework was shown to be helpful in analysing and addressing the limitations of 4D light field depth estimation. For that purpose, a novel approach (IOADR) is proposed, based on a local optimisation method for depth estimation with three significant contributions: a novel occlusion detection algorithm capable of delivering occlusion-aware disparity estimation

Table V: Objective Metric Comparison with State-of-the-Art methods. Shaded cells indicate learning-based methods. The best result for each light field is in italics. The best non-learning-based result for each light field is in bold.

	Boxes	Cotton	Dino	Sideboard
	MSE × 100			
EPINet [8]	6.24	0.191	0.167	0.827
AttNet [9]	<i>3.842</i>	<i>0.059</i>	<i>0.045</i>	<i>0.398</i>
Ober-Cross + ANP [24]	4.750	0.555	0.336	<b>0.941</b>
Ober-Cross [24]	<b>4.160</b>	0.501	<b>0.309</b>	0.963
OFSY [46]	9.561	2.653	0.782	2.478
IOADR (Ours)	4.601	<b>0.375</b>	0.319	0.962
	Badpix 0.07			
EPINet [8]	12.34%	0.45%	1.21%	4.46%
AttNet [9]	11.14%	<i>0.20%</i>	<i>0.44%</i>	<i>2.69%</i>
Ober-Cross + ANP [24]	<b>10.76%</b>	1.02%	2.07%	<b>5.67%</b>
Ober-Cross [24]	13.13%	<b>0.94%</b>	<b>1.95%</b>	6.28%
OFSY [46]	19.25%	3.04%	3.43%	10.36%
IOADR (Ours)	15.53%	2.21%	3.09%	8.01%
	MAE in planar regions			
EPINet [8]	9.544	49.378	6.032	10.631
AttNet [9]	5.819	10.472	2.686	6.078
Ober-Cross + ANP [24]	5.402	12.674	3.062	6.219
Ober-Cross [24]	8.894	15.951	4.893	12.083
OFSY [46]	3.574	2.909	1.069	4.151
IOADR (Ours)	<b>1.819</b>	<b>2.885</b>	<b>0.593</b>	<b>3.706</b>

with accurate boundaries, a new algorithm for estimating accurate surface normals from noisy depth estimations, and a cost term capable to evaluate for each depth value candidate its suitability to be a good fit relative to the local surface normals.

The proposed framework presents very competitive results regarding MSE when compared to other non-learning-based methods. In terms of MAE in planar regions, the framework achieves, by far, the best results in the state-of-the-art, comprising both non-learning-based and learning-based methods, obtaining good results in the planar areas without overly compromising the accuracy of the disparity map. On average, for the MAE metric, the proposed method obtains, on average, a gain of 26.3% relative to the second-best method.

It is important to note that the mathematical framework formalised in this paper may bring valuable insights for the development of both learning and non-learning-based methods. For instance, the proposed cost model in Eq. (23) may be readily incorporated into a learning-based architecture.

## REFERENCES

- [1] P. Cipresso, I. A. C. Giglioli, M. A. Raya, and G. Riva, “The past, present, and future of virtual and augmented reality research: A network and cluster analysis of the literature,” *Frontiers in Psychology*, vol. 9, 2018.
- [2] S. Dargan, S. Bansal, M. Kumar, A. Mittal, and K. Kumar, “Augmented reality: A comprehensive review,” *Archives of Computational Methods in Engineering*, vol. 30, no. 2, pp. 1057–1080, Mar 2023.
- [3] Raytrix-GmbH, “3D optical inspection,” <https://raytrix.de/inspection/>, 2018, accessed: 2018-11-30.
- [4] D. Liu, R. Nicolescu, and R. Klette, “Bokeh effects based on stereo vision,” in *Computer Analysis of Images and Patterns*, G. Azzopardi and N. Petkov, Eds. Cham: Springer International Publishing, 2015, pp. 198–210.

- [5] P. M. M. Pereira, L. A. Thomaz, L. M. N. Tavora, P. A. A. Assunção, R. Fonseca-Pinto, R. P. Paiva, and S. M. M. Faria, "Multiple instance learning using 3D features for melanoma detection," *IEEE Access*, vol. 10, pp. 76 296–76 309, 2022.
- [6] D. Scharstein and R. Szeliski, "High-accuracy stereo depth maps using structured light," in *Conference on Computer Vision and Pattern Recognition*, vol. 1, 2003.
- [7] Z. Wang and M. Menenti, "Challenges and opportunities in lidar remote sensing," *Frontiers in Remote Sensing*, vol. 2, 2021.
- [8] C. Shin, H.-G. Jeon, Y. Yoon *et al.*, "Epinet: A fully-convolutional neural network using epipolar geometry for depth from light field images," in *Conference on Computer Vision and Pattern Recognition*, Salt Lake City, UT, USA, June 2018.
- [9] Y.-J. Tsai, Y.-L. Liu, M. Ouhyoung, and Y.-Y. Chuang, "Attention-based view selection networks for light-field disparity estimation," *AAAI Conference on Artificial Intelligence*, vol. 34, pp. 12 095–12 103, Apr. 2020.
- [10] K. Li, J. Zhang, R. Sun, X. Zhang, and J. Gao, "Epi-based oriented relation networks for light field," in *British Machine Vision Conference*, September 2020.
- [11] W. Yan, X. Zhang, H. Chen, C. Ling, and D. Wang, "Light field depth estimation based on channel attention and edge guidance," in *2022 China Automation Congress*, 2022, pp. 2595–2600.
- [12] L. Han, S. Zheng, Z. Shi, and M. Xia, "Exploiting sequence analysis for accurate light-field depth estimation," *IEEE Access*, vol. 11, pp. 74 657–74 670, 2023.
- [13] S. Zhang, N. Meng, and E. Y. Lam, "Unsupervised light field depth estimation via multi-view feature matching with occlusion prediction," *IEEE Transactions on Circuits and Systems for Video Technology*, pp. 1–1, 2023.
- [14] O. Johannsen, K. Honauer, B. Goldluecke *et al.*, "A taxonomy and evaluation of dense light field depth estimation algorithms," in *Conference on Computer Vision and Pattern Recognition Workshops*, Honolulu, USA, July 2017, pp. 1795–1812.
- [15] D. Dansereau and L. Bruton, "Gradient-based depth estimation from 4D light fields," in *International Symposium on Circuits and Systems*, vol. 3, 2004, pp. III–549.
- [16] S. Wanner and B. Goldluecke, "Globally consistent depth labeling of 4D light fields," in *Conference on Computer Vision and Pattern Recognition*, Providence, USA, June 2012, pp. 41–48.
- [17] J. Li and Z. N. Li, "Continuous depth map reconstruction from light fields," in *IEEE International Conference on Multimedia and Expo*, July 2013, pp. 1–6.
- [18] J. Li, M. Lu, and Z. Li, "Continuous depth map reconstruction from light fields," *IEEE Transactions on Image Processing*, vol. 24, no. 11, pp. 3257–3265, November 2015.
- [19] R. Lourenco, P. A. A. Assunção, L. M. N. Tavora, R. Fonseca-Pinto, and S. M. M. Faria, "Silhouette enhancement in light field disparity estimation using the structure tensor," in *International Conference on Image Processing*, Athens, Greece, October 2018, pp. 2580–2584.
- [20] R. M. Lourenco, L. M. N. Tavora, P. A. A. Assunção, L. A. Thomaz, R. Fonseca-Pinto, and S. M. M. Faria, "Enhancement of light field disparity maps by reducing the silhouette effect and plane noise," *Multidimensional Systems and Signal Processing*, Jan 2022.
- [21] N. Khan, M. H. Kim, and J. Tompkin, "Edge-aware bidirectional diffusion for dense depth estimation from light fields," in *British Machine Vision Conference*, 2021.
- [22] J. Y. Lee and R.-H. Park, "Complex-valued disparity: Unified depth model of depth from stereo, depth from focus, and depth from defocus based on the light field gradient," *IEEE Transactions on Pattern Analysis and Machine Intelligence*, vol. 43, no. 3, pp. 830–841, 2021.
- [23] S. Zhang, H. Sheng, C. Li *et al.*, "Robust depth estimation for light field via spinning parallelogram operator," *Computer Vision and Image Understanding*, vol. 145, pp. 148–159, 2016.
- [24] H. Schilling, M. Diebold, C. Rother, and B. Jähne, "Trust your model: Light field depth estimation with inline occlusion handling," in *Conference on Computer Vision and Pattern Recognition*, Salt Lake City, UT, USA, June 2018, pp. 4530–4538.
- [25] M. W. Tao, S. Hadap, J. Malik, and R. Ramamoorthi, "Depth from combining defocus and correspondence using light-field cameras," *IEEE International Conference on Computer Vision*, pp. 673–680, March 2013.
- [26] H. G. Jeon, J. Park, G. Choe *et al.*, "Accurate depth map estimation from a lenslet light field camera," in *Conference on Computer Vision and Pattern Recognition*, Boston, USA, June 2015, pp. 1547–1555.
- [27] H. Lin, C. Chen, S. Bing Kang, and J. Yu, "Depth recovery from light field using focal stack symmetry," *International Conference on Computer Vision*, December 2015.
- [28] T.-C. Wang, A. A. Efros, and R. Ramamoorthi, "Depth estimation with occlusion modeling using light-field cameras," *IEEE Transactions on Pattern Analysis and Machine Intelligence*, vol. 38, no. 11, pp. 2170–2181, 2016.
- [29] W. Williem and I. K. Park, "Robust light field depth estimation for noisy scene with occlusion," in *Conference on Computer Vision and Pattern Recognition*, Las Vegas, USA, 2016, pp. 4396–4404.
- [30] M. Strecke, A. Alperovich, and B. Goldluecke, "Accurate depth and normal maps from occlusion-aware focal stack symmetry," in *Computer Vision and Pattern Recognition*, Honolulu, USA, July 2017, pp. 2529–2537.
- [31] W. Williem, I. K. Park, and K. M. Lee, "Robust light field depth estimation using occlusion-noise aware data costs," *IEEE Transactions on Pattern Analysis and Machine Intelligence*, pp. 1–1, August 2018.
- [32] S. Ma, Z. Guo, J. Wu *et al.*, "Occlusion-aware light field depth estimation using side window angular coherence," *Appl. Opt.*, vol. 60, no. 2, pp. 392–404, Jan 2021.
- [33] K. Han, W. Xiang, E. Wang, and T. Huang, "A novel occlusion-aware vote cost for light field depth estimation," *IEEE Transactions on Pattern Analysis and Machine Intelligence*, pp. 1–1, 2021.
- [34] M. Levoy and P. Hanrahan, "Light field rendering," in *Proceedings of the 23rd Annual Conference on Computer Graphics and Interactive Techniques*, ser. SIGGRAPH '96. New York, NY, USA: Association for Computing Machinery, 1996, p. 31–42.
- [35] M. B. de Carvalho, C. L. Pagliari, G. O. e Alves, C. Schretter, P. Schelkens, F. Pereira, and E. A. B. da Silva, "Supporting wider baseline light fields in jpeg pleno with a novel slanted 4D-DCT coding mode," *IEEE Access*, vol. 11, pp. 28 294–28 317, 2023.
- [36] J. Bigun, "Optimal orientation detection of linear symmetry," in *IEEE First International Conf. on Computer Vision*, London, Great Britain, June 1987, pp. 433–438.
- [37] L. I. Rudin, S. Osher, and E. Fatemi, "Nonlinear total variation based noise removal algorithms," *Physica D: Nonlinear Phenomena*, vol. 60, no. 1, pp. 259–268, 1992.
- [38] M. Ruzon and C. Tomasi, "Color edge detection with the compass operator," in *Conference on Computer Vision and Pattern Recognition*, vol. 2, June 1999, pp. 160–166 Vol. 2.
- [39] E. J. Kirkland, *Bilinear Interpolation*. Boston, MA: Springer US, 2010, pp. 261–263.
- [40] W. Zhou, L. Lin, Y. Hong, Q. Li, X. Shen, and E. E. Kuruoglu, "Beyond photometric consistency: Geometry-based occlusion-aware unsupervised light field disparity estimation," *IEEE Transactions on Neural Networks and Learning Systems*, pp. 1–15, July 2023.
- [41] Y. Nakagawa, H. Uchiyama, H. Nagahara, and R.-I. Taniguchi, "Estimating surface normals with depth image gradients for fast and accurate registration," in *2015 International Conference on 3D Vision*, 2015, pp. 640–647.
- [42] M. Gutsche, H. Schilling, M. Diebold, and C. Garbe, "Surface normal reconstruction from specular information in light field data," in *Conference on Computer Vision and Pattern Recognition Workshops*, July 2017, pp. 1735–1742.
- [43] Z. Cui, H. Sheng, D. Yang, S. Wang, R. Chen, and W. Ke, "Light field depth estimation for non-lambertian objects via adaptive cross operator," *IEEE Transactions on Circuits and Systems for Video Technology*, pp. 1–1, 2023.
- [44] D. Bertsimas and J. Tsitsiklis, "Simulated annealing," *Statistical science*, vol. 8, no. 1, pp. 10–15, 1993.
- [45] S. Kirkpatrick, C. D. Gelatt, and M. P. Vecchi, "Optimization by simulated annealing," *Science*, vol. 220, no. 4598, pp. 671–680, 1983.
- [46] M. Strecke and B. Goldluecke, "Sublabel-accurate convex relaxation with total generalized variation regularization," in *German Conference on Pattern Recognition (Proc. GCPR)*, 2018.